Anomalous lattice tilting across a magnetic oxide heterostructure

P. F. Chen,[1,2] D. Lan,[2] Y. Y. Li,[3] P. Yang,[4] X. J. Yu,[4] K. Han,[1] L. Q. Xu,[1] J. W. Huang,[1] J. S. Chen,[2] G. M. Chow,[2,*] W. B. Wu,[5,†] and Z. Huang[1,6,‡]

[1]*Information Materials and Intelligent Sensing Laboratory of Anhui Province, Institutes of Physical Science and Information Technology, Anhui University, Hefei, Anhui, 230601, People's Republic of China*

[2]*Department of Materials Science and Engineering, National University of Singapore, 117575, Singapore*

[3]*School of Physics, Shandong University, Jinan, Shandong, 250100, People's Republic of China*

[4]*Singapore Synchrotron Light Source (SSLS), National University of Singapore, 5 Research Link, 117603, Singapore*

[5]*Hefei National Laboratory for Physical Sciences at Microscale, University of Science and Technology of China, Hefei 230026, People's Republic of China*

[6]*Stony Brook Institute at Anhui University, Anhui University, Hefei 230039, People's Republic of China*

(Received 15 June 2022; accepted 16 September 2022; published 28 September 2022)

It is well known that the conventional lattice flexibility of an epitaxial layer is restricted by its growth template and bulk counterpart. Here, we report that the interface-engineered (La,Ca)MnO_3 layer can exhibit an anomalous lattice-tilting pattern, featured by the interaxis angle α that exceeds the range of the lattice flexibility mentioned earlier. By increasing the adjacent $CaRuO_3$ layer thickness, the (La,Ca)MnO_3 layer shows a decreasing α down to 89.25°, which is out of the flexible range between 93.82° (from the $CaRuO_3$ template) and 89.86° [from the (La,Ca)MnO_3 bulk]. The resulting antiparallel lattice tilting makes the (La,Ca)MnO_3/$CaRuO_3$ interface similar to a crystal twinning plane to lower the interfacial energy raised by the structural discontinuity. Also, a monotonic reduction of magnetic coercivity (from 205 to 70 Oe) is observed on decreasing α (from 90° to 89.25°) in (La,Ca)MnO_3 layers, providing an additional approach to tunable magnetic properties without changing the epitaxial strain. Our results not only present a new lattice-engineering strategy of using the interface similar to a crystal-twinning plane in designing heterostructures, but also they reveal the application of such a strategy for tunable magnetic properties beyond the epitaxial strain.

DOI: 10.1103/PhysRevMaterials.6.094414

I. INTRODUCTION

Template-induced lattice modification provides an effective approach to tunable functionalities in heterostructures [1–4]. In the conventional concept of structural evolution, the lattice parameters of an epitaxial layer are usually modulated within the range defined by its growth template and bulk counterpart, corresponding to the strained state (with a small misfit or the layer thickness below the critical thickness) and the relaxed state (with a large misfit or the layer thickness above the critical thickness) in a heterostructure with lattice mismatch [5–11]. Recent attempts have been made to establish the novel lattice structures that cannot be induced by conventional epitaxial strain, aiming to expand the function tunability of thin layers [12–18]. One strategy is to free the layer from the template, i.e., to remove the epitaxial strain on the layer. Thanks to the soluble $Sr_3Al_2O_6$-based sacrificial layer, the freestanding functional oxide layer becomes achievable, leading to expanded lattice flexibility with novel magnetic and ferroelectric properties [12–17]. However, this method requires complicated procedures, including sacrificial-layer etching and functional-layer transferring, and thus may be not suitable for obtaining high-quality layers with a large size. Another idea is to realize the unconventional lattice structure without removing its growth template [18]. As plotted in Fig. 1(a), when a material (with its lattice length a_B) is grown on a substrate (with the lattice length a_S) under a tensile strain (i.e., $a_S > a_B$), the conventional flexibility of the in-plane lattice length a of the layer shall be within a range of $a_S \geqslant a \geqslant a_B$ [7,19,20]. By contrast, Fig. 1(b) shows one anomalous case where the shrinkage of in-plane lattices is intuitively against the tensile strain. Similarly, if focusing on lattice tilting indexed by the interaxis angle α, Fig. 1(c) displays a normal heterostructure with the layer's α being confined by its substrate's α_S and bulk counterpart's α_B (i.e., $\alpha_S \geqslant \alpha \geqslant \alpha_B$) [21–23], while the anomalous α of $\alpha < \alpha_B$ is sketched in Fig. 1(d). Although those unconventional structures plotted in Fig. 1(b) and 1(d) can ideally expand lattice flexibility, it is challenging to build such lattices experimentally that contradict the conventional concept of lattice evolution in an epitaxial layer. Hence, other interfacial mechanisms must be utilized to fulfil those anomalous structural modulations.

Recent studies have revealed that the collective rotation of corner-shared oxygen octahedra enriches the lattice diversity in epitaxial perovskite oxide layers [24–32]. Usually, in the epitaxial layer, the oxygen octahedral rotation (OOR) is clamped by the template within 2 to 4 unit cells (u.c.)

*msecgm@nus.edu.sg
†wuwb@ustc.edu.cn
‡huangz@ahu.edu.cn

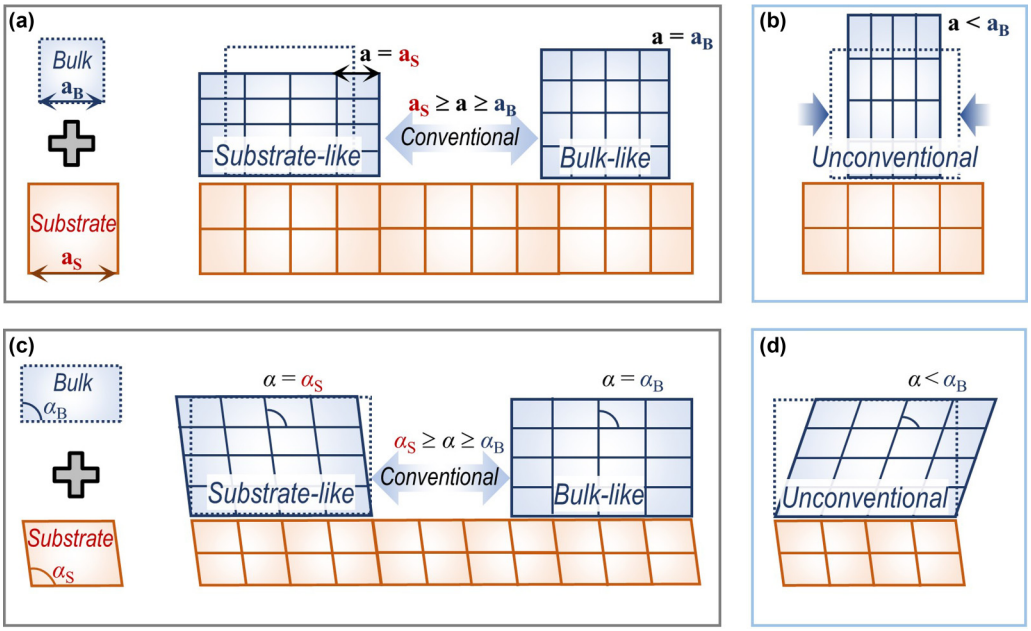

FIG. 1. The sketches for conventional and unconventional lattice flexibility. Under a tensile strain, the sketch of the layer lattice length a with the conventional flexibility of $a_S \geqslant a \geqslant a_B$ is plotted in (a), and unconventional $a < a_B$ in (b). For lattice tilting, the sketch of the layer interaxis angle α with the conventional flexibility of $\alpha_S \geqslant \alpha \geqslant \alpha_B$ is plotted in (c), and unconventional $\alpha < \alpha_B$ in (d). The dashed rectangles represent the bulk counterpart's lattice for the layer.

close to the interface, and then becomes gradually relaxed to the bulk-like style when the layer is thick. Such gradual relaxation of the OOR can induce some metastable lattice structures without changing the epitaxial strain; however, most OOR-mediated structural modifications in previous studies are similar to the epitaxial strain–induced ones, and thus are still confined by the growth template and bulk counterpart [33–35]. In this work, the magnetic layer of $La_{2/3}Ca_{1/3}MnO_3$ (LCMO) is selected as the functional layer to present the anomalous lattice-tilting modifications that is beyond the lattice flexibility suggested by a conventional epitaxial heterostructure. The nonmagnetic $CaRuO_3$ (CRO) layer and $NdGaO_3$ (NGO) crystal are used as growth templates. For their bulk counterparts, CRO, LCMO, and NGO share a similar *Pbnm* orthorhombic $A_4B_4O_{12}$ lattice, or a pseudocubic ABO_3 lattice with the OOR pattern of $c^+a^-a^-$ indexed by Glazer notation [36,37]. As plotted in Supplemental Material Fig. S1 [38], the conversion between pseudocubic lattice constants (a, b, and c; α, β, and γ) and orthorhombic ones (a_{Or}, b_{Or}, and c_{Or}) can be expressed as $a = c_{Or}/2$, $b = c = (a_{Or}{}^2 + b_{Or}{}^2)^{0.5}/2$, $\alpha = 2\tan^{-1}(b_{Or}/a_{Or})$, and $\beta = \gamma = 90^\circ$. If using the pseudocubic ABO_3 lattice, the lattice parameters can be written as $a = 3.856$ Å, $b = c = 3.865$ Å, $\alpha = 89.86^\circ$, and $\beta = \gamma = 90^\circ$ for LCMO [6]; $a = 3.776$ Å, $b = c = 3.779$ Å, $\alpha = 93.82^\circ$, and $\beta = \gamma = 90^\circ$ for CRO [39]; and $a = 3.858$ Å, $b = c = 3.867$ Å, $\alpha = 90.73^\circ$, and $\beta = \gamma = 90^\circ$ for NGO [6,40]. In other words, the monoclinic-like distortion in the pseudocubic ABO_3 lattice can be identified by the interaxis angle $\alpha \neq 90^\circ$. Based on this structural information, layer-by-layer coherent growth may be maintained because of the close lattice lengths in CRO/LCMO/CRO//NGO trilayers (see Supplemental Material Fig. S2 [38]). In addition, if the bulk-like α is maintained (i.e., $89.86^\circ \leqslant \alpha < 90^\circ$ in LCMO and $90^\circ < \alpha \leqslant 90.73^\circ$ in CRO), the antiparallel lattice-tilting pattern with a twin-like lattice symmetry at the LCMO/CRO heterointerface is expected (see Supplemental Material Fig. S3 [38]).

II. EXPERIMENTS

A. Sample Preparation

All our LCMO/CRO heterostructures were fabricated on the $(110)_{Or}$-oriented $NdGaO_3$ substrates by pulsed laser deposition. During the deposition, the growth temperature was kept at 700 °C, the oxygen partial pressure at 40 Pa, and the laser energy at 2 J/cm^2. The layer thickness was monitored *in situ* by reflection high-energy electron diffraction. After deposition, samples were annealed *in situ* for 15 min before being cooled down in the same deposition atmosphere.

B. Characterization on the Lattice Structure and OOR

The crystallographic structures were probed by half-integer X-ray diffraction (XRD) and reciprocal space mappings (RSMs) using high-resolution XRD with $CuK_{\alpha 1}$ radiation ($\lambda = 1.5406$ Å, PANalytical, X' pert) and the Huber four-circle diffractometer system 90000–0216/0 at the Singapore Synchrotron Light Source (SSLS).

C. Magnetic Measurements

Magnetic properties were measured using a superconducting quantum interference device vibrating sample magnetometer (SQUID-VSM, Quantum Design). For the temperature-dependent magnetic moment, the sample was first cooled to 10 K under a magnetic field of 3000 Oe, and then measured during the warming process under 200 Oe. For

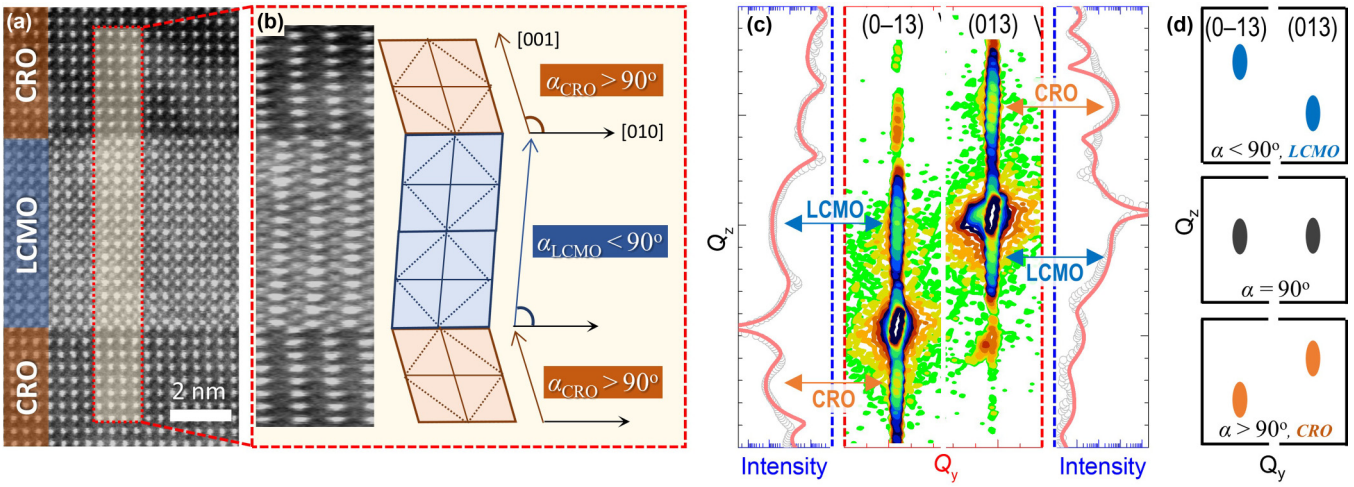

FIG. 2. Conventional lattice tilting in thick LCMO layers. (a) The STEM image for CRO/LCMO/CRO//NGO. The layer thickness is 32 u.c. for the CRO buffer layer, 15 u.c. for LCMO, and 16 u.c. for CRO capping. (b) The modified STEM image, which is horizontally stretched by three times compared to the original area highlighted in (a). (c) RSMs around (0±13) reflections of LCMO/CRO//NGO. The asymmetric reflections for CRO and LCMO are indicated by orange and blue arrows, respectively. Also, the corresponding L scans (gray open circles) and fitting curves (red lines) are compared at both sides of (c). Here, Q_y and Q_z stand for $\lambda/2b$ and $3\lambda/2c$, where λ is the wavelength of X-ray (1.5406 Å) [39,44]. (d) Relationship between the asymmetric (0±13) reflections and lattice tilting.

the field-dependent magnetic moment, the sample was first zero-field-cooled to the target temperature and then measured.

D. Scanning Transmission Electron Microscopy

The cross-sectional sample for the scanning transmission electron microscopy (STEM) analysis was prepared by a focused ion beam (FEI Helios 400S). A transmission electron microscopy lamella was transferred to a half-moon focused ion beam grid first by the *in situ* lift-out method, then cleaned by a low-voltage argon ion beam in the Fischione NanoMill 1040. The cross-section of the trilayer structure was characterized by the Mono-Probe Cs scanning transmission electron microscope (Titan, FEI), operated at 300 kV.

III. RESULTS AND DISCUSSIONS

A. Bulk-like Lattice Tilting of Heterostructures with Thick LCMO Layers

Figure 2 shows the experimental results on lattice characteristics for LCMO/CRO heterostructures with thick LCMO layers (16 and 60 u.c.), of which the interface shows a twin-like symmetry of lattice tilting as discussed earlier. In Fig. 2(a) and 2(b), the STEM images clearly demonstrate the inclined directions of the c-axis (or [001]) are antiparallel in the LCMO and CRO layers (see also Supplemental Material Fig. S4 and S5 [38]). The out-of-plane c-axis is inclined to the b (or [010]) and $-b$ (or [0–10]) axis in the LCMO and CRO layers, respectively. This antiparallel lattice tilting corresponds to $\alpha_{LCMO} < 90°$ and $\alpha_{CRO} > 90°$ in two adjacent layers, creating a twin-like lattice symmetry across the LCMO/CRO interface. Besides the atomic images in the real space, the nonorthogonal axes with $\alpha \neq 90°$ can be also indexed by the asymmetric diffraction spots using X-ray RSMs [6,23,41–43]. In Fig. 2(c), the RSMs around (0±13) reflections of the thick LCMO/CRO heterostructure are compared. The peak positions are fitted by taking the interlayer coherent interferences into consideration [44,45]. The corresponding results are shown at two sides of Fig. 2(c) (see Supplemental Material Fig. S6 [38]). First, both the LCMO and CRO layers (indicated by blue and orange arrows, respectively) share the same in-plane projection of Q_y with their substrate NGO, confirming the coherent growth and identical in-plane lattice constant across the entire heterostructure. Second, compared to the (013) reflection, the (0−13) reflection of the LCMO layer exhibits the higher out-of-plane projection of Q_z (or $Q_{z,0-13} > Q_{z,013}$), while the CRO layer and NGO substrate show the lower Q_z of (0−13) (or $Q_{z,0-13} < Q_{z,013}$). The correspondence between the symmetry of (0±13) reflections and the orthogonality between b- and c-axis is illustrated in Fig. 2(d). Accordingly, the inclined angle $\Delta\alpha$ can be calculated using either $\Delta\alpha = 90° - \alpha = 90° - 2\tan^{-1}(b_{Or}/a_{Or})$ in the real space or $\Delta\alpha = \tan^{-1}[(Q_{z,0-13} - Q_{z,013})/|2Q_y|]$ in the reciprocal space [41,46]. A detailed analysis can be found in Supplemental Material Fig. S7 [38]. Hence, the LCMO and CRO layers show the α of 89.83° and 91.81°, consistent with the antiparallel lattice tilting across the LCMO/CRO interface recorded in the STEM results. It must be noted that, given the measurement uncertainty of $\alpha(\sim \pm 0.02°)$, those α values for the thick LCMO and CRO layers are still within the range of conventional lattice flexibility, i.e., $89.86° \leqslant \alpha \leqslant 93.82°$, defined by the LCMO and CRO bulk counterparts [23,39].

B. Anomalous Lattice Tilting of Heterostructures with Thin LCMO Layers

Now we focus on building the unconventional lattice tilting in CRO(y)/LCMO/CRO(x) trilayers, where the thickness of the magnetic LCMO layer is always fixed at 8 u.c. and x (y) stands for the variable thickness of the CRO buffer (capping) layer. Here, unlike the LCMO single layer that cannot maintain the ferromagnetic ground state under 8 u.c.,

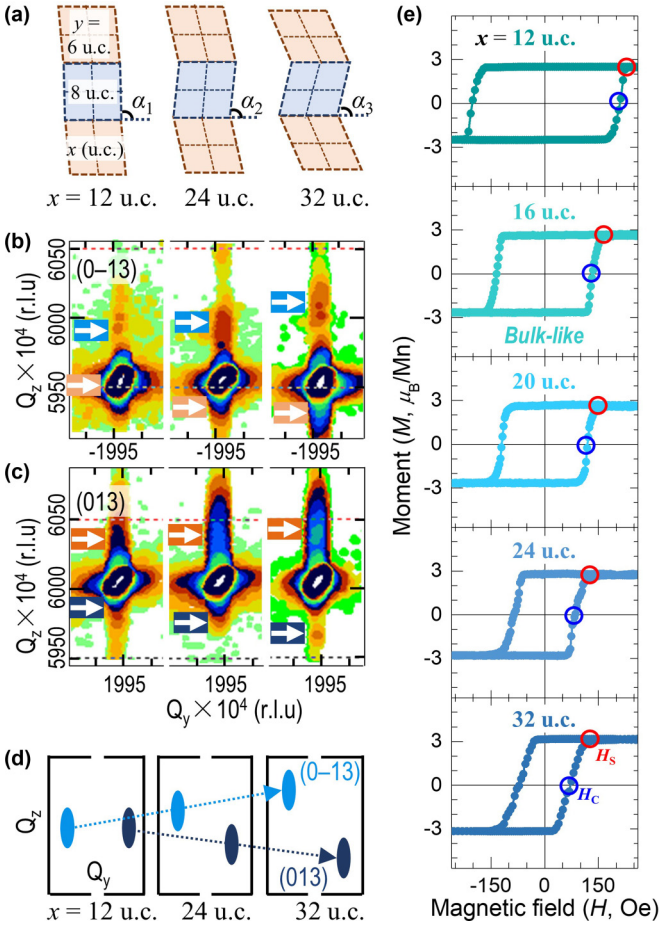

FIG. 3. Unconventional lattice tilting in ferromagnetic 8-u.c. LCMO layers. (a) The sketches for x-dependent monoclinic-like lattice tilting of trilayers. (b) and (c) RSMs around (0±13) reflections for CRO/LCMO/CRO//NGO with different x. The asymmetric reflections of LCMO and CRO are indicated by blue and orange arrows, respectively. (d) The evolution of the LCMO (0±13) reflections on x (from 12 to 32 u.c.). (e) M-H hysteresis loops measured at 150 K for trilayers with x from 12 to 32 u.c.; H_C and H_S are denoted by blue and red circles, respectively.

the CRO-sandwiched LCMO layer can show the bulk-like ferromagnetism down to 4 u.c. due to the interlayer charge transfer of LCMO/CRO [39,47]. Figure 3(a) sketches the effect of the CRO buffer layer on modifying the lattice tilting of LCMO by changing the buffer layer x from 12 to 32 u.c. and keeping the capping layer y at 6 u.c. in all samples. On increasing x, the CRO layer shows an enhanced monoclinic-like lattice tilting, which is reflected by the increasing α that is more than 90°. This can be understandable because the value of α in a thick CRO layer is approaching its bulk value of 93.82°. Meanwhile, the LCMO layer with a fixed layer thickness also exhibits a strengthened lattice tilting, but with an antiparallel inclined direction, featured by the decreasing α that is less than 90°. The experimental evidence can be seen in Fig. 3(b) and 3(c). The increasing x results in the lifted Q_z for LCMO (0−13) reflection and lowered Q_z for LCMO (013) (indicated by blue arrows), while the opposite trend is observed for the CRO layer (indicated by orange arrows). The more asymmetric (0±13) reflections correspond to the more inclined lattices. The evolution of LCMO (0±13) reflections are illustrated in Fig. 3(d). For the x = 12 u.c. sample, the (0±13) reflections of the LCMO layer are almost symmetric, revealing an almost nontilted ABO_3 lattice with $\alpha \sim 90°$. Based on the corresponding L scans in Supplemental Material Fig. S8 [38], $\Delta\alpha$ is only around 0.04 ° close to our measurement uncertainty. When increasing x to 24 and 32 u.c., the sandwiched 8-u.c.-thick LCMO layer shows α gradually decreased down to 89.66° and 89.34°, respectively. Those values of α are clearly out of the range of $89.86° \leqslant \alpha \leqslant 93.82°$, which is expected in the conventional lattice evolution in the LCMO/CRO heterostructure. By contrast, it shall be noted that the CRO layer is still within the conventional lattice-flexibility range, with α changing from 91.10 ° to 91.45 ° on increasing x. Apparently, the evolution of LCMO lattice tilting on x is not in line with the conventional concept of structural evolution in an epitaxial heterostructure. When the in-plane lattice length of the LCMO layer is still fully strained to the growth template, the interaxis angle α of LCMO seems to be already "relaxed," or even "over-relaxed," to 89.66 ° and 89.34 °, which break the confinement of lattice flexibility set by its own bulk counterpart of $\alpha \geqslant 89.86°$. Therefore, a new mechanism shall play an important role here.

More interestingly, Fig. 3(e) compares the magnetic-field-dependent moments ($M-H$) measured at 150 K for those trilayers. Given that all the sandwiched 8-u.c.-thick LCMO layers exhibit the similar bulk-like Curie temperature T_C around 255 K (see more details in Supplemental Material Fig. S9 [38]), the ferromagnetic phase must dominate the ground state. This is different from the case of the LCMO single layer, and the interlayer charge transfer makes the LCMO/CRO interface an ideal platform to study the magnetic modulations induced by the interfacial effect that fades rapidly in a thick layer [39,47]. The increase of x not only triggers the unconventional lattice tilting (x > 16 u.c.), but also effectively reduces the magnetic coercivity H_C, as well as the saturated field H_S, in those LCMO thin layers. Specifically, H_C is reduced one third (from 205 to 70 Oe), when increasing x from 12 to 32 u.c., or reducing α from $\sim$ 90° to 89.34 °. On the other hand, the saturated magnetic moment ($\sim 3\,\mu_B$/Mn) is almost unchanged in all samples. Given the experimental observations of correlated α and H_C, a possible linkage between the lattice tilting and magnetic hardness may exist in those ferromagnetic LCMO layers.

C. Possible Mechanisms for Anomalous Lattice Tilting

Although unconventional lattice tilting has been clearly demonstrated in the interface-engineered LCMO layers, two key questions are still left for further discussion. One is: Which interfacial mechanism may be responsible for such lattice tilting beyond the lattice flexibility suggested by a conventional heterostructure? And the other is: How is the magnetic coercivity influenced by this lattice tilting in perovskite oxide layers?

To propose a possible mechanism, the roles of crystal twinning and OOR are highlighted. First, structural similarities can be found if comparing the LCMO/CRO heterostructures with twinned crystals. Generally, for the twinned crystals,

two structural domains are separated by one twinning plane; the atoms hosted by the twinning plane are simultaneously shared by two domains to lower the boundary energy; and the additional twin symmetry, which does not belong to the untwinned crystal, is formed across the twinning plane [48–50]. Similarly, the LCMO/CRO interface divides the heterostructure into two individual layers (i.e., the LCMO layer and the CRO layer) with similar lattice symmetry; they share all the atoms at the interface due to the coherent growth. Owing to the antiparallel inclined direction, a twin-like symmetry of lattice tilting is well established crossing the LCMO/CRO interface. That is to say, if taking a reference from the crystal twinning, the coherently grown LCMO and CRO layers can be viewed as two structural domains coexisting in one crystal. The LCMO/CRO interface may serve as a twinning plane, reducing the energy raised by the structural discontinuity between the LCMO and CRO layers with the twin-like lattice structure, as discussed later.

The total interfacial energy can be divided into two parts: One is the interfacial energy due to the structural difference between the LCMO layer and the LCMO bulk, and the other one is the energy contribution from the lattice difference between the LCMO layer and the adjacent CRO template. When compared with the LCMO bulk alone, an energy minimum can be reached when the lattice tilting of the LCMO layer follows its bulk's pattern (with $\alpha = \alpha_{\mathrm{LCMO}}$). Similarly, the energy contribution from the CRO template will be lowest if the LCMO layer follows the CRO lattice-tilting pattern (with $\alpha = \alpha_{\mathrm{CRO}}$) with minimal structural discontinuity across the heterointerface. However, there is one more local energy minimum where the twin-like lattice is formed (with $\alpha = 180^\circ - \alpha_{\mathrm{CRO}}$), and both the LCMO and CRO layers show similar lattice symmetry. It is true that the twin-like structure has the higher CRO's energy contribution than the case of $\alpha = \alpha_{\mathrm{CRO}}$ due to the existence of the twin-like plane at the interface. However, the case of $\alpha = 180^\circ - \alpha_{\mathrm{CRO}}$ exhibits the lower CRO's energy contribution compared to other lattice tilting states with $\alpha \neq \alpha_{\mathrm{CRO}}$ or $180^\circ - \alpha_{\mathrm{CRO}}$, where a similar twin-like plane is formed for all cases, and the LCMO and CRO layers exhibit larger differences in lattice symmetry. Hence, the total interfacial energy can be qualitatively estimated by summing up both energy contributions, and α with the lowest total interfacial energy may stay within the range of $180^\circ - \alpha_{\mathrm{CRO}} < \alpha < \alpha_{\mathrm{LCMO}}$, as shown in Supplemental Material Fig. S10 [38].

Second, the concept of crystal twinning could lead to the lattice modification, which is different from the one expected from the conventional heterostructures. With the conventional scenario, the CRO-sandwiched LCMO layer should follow the CRO's lattice-tilting pattern, i.e., α in both the CRO and LCMO layers should simultaneously increase or decrease with respect to the buffer layer thickness x. On the contrary, if following the concept of crystal twinning, the twin-like symmetry of lattice tilting shall be always maintained, leaving the opposite trends of α modulations with x. In other words, based on the crystal-twinning model, the more α increases in the CRO layer ($> 90^\circ$), the more α reduces in LCMO layer ($< 90^\circ$). Our experimental results shown in Fig. 3(a)–3(d) confirm the antiparallel inclined directions across the LCMO/CRO interface on increasing x. When α increases from 91.10 ° to 91.45 ° in the CRO layer ($> 90^\circ$), α decreases from 89.96 ° to 89.34°($< 90^\circ$) in the LCMO layer. The observed opposite trends in the LCMO and CRO layers support the validity of the crystal-twinning model. Also, this may explain why unconventional lattice tilting can be achieved in the LCMO/CRO heterostructure.

Third, OOR may be able to bridge the gap between coherent growth and unconventional lattice tilting [51,52]. Previous studies have shown that the strain relaxation can cause the crystal twinning in one single layer, where the random distribution of twinning domains may be difficult to utilize to design novel lattice structures artificially [53–55]. However, in the LCMO/CRO heterostructure, lattice tilting with nonorthogonal crystal axes can be induced by OOR, creating a twin-like symmetry without breaking the coherent growth at the heterointerface. Figure 4(a)–4(c) demonstrates how the out-of-phase rotations, which are applied along the b- and c-axes with the rotation angle ω_b and ω_c, cause the lattice tilting with $\alpha \neq 90^\circ$. In Fig. 4(a), the octahedral rotations start with a nonrotated ABO_3 lattice network with the OOR pattern of $a^0a^0a^0$ and a lattice constant of l. When the out-of-phase rotations are applied along the c-axis, the OOR pattern changes to $a^0a^0c^-$. In this case, the oxygen atoms that connect oxygen octahedra along the b-axis (highlighted by dash circles) will be shifted by a distance of $\delta_a = l/2 \times \sin\omega_c$ along the [100] or [−100] alternatively, while the orthogonality between the b- and c-axes is still maintained with $\alpha = 90^\circ$. If additional out-of-phase rotations are applied along the b-axis for $a^0b^-c^-$, extra displacements along [00−1] will be induced on those oxygen atoms with dash circles, resulting in the lattice tilting ($\alpha \neq 90^\circ$) with an inclined angle $\Delta\alpha$ of $\tan|\Delta\alpha| = 2\delta_z/l = \sin\omega_b \times \sin\omega_c$. Hence, lattice tilting (indexed by α or $\Delta\alpha$) can be quantitatively related to the OOR (indexed by ω_b and ω_c). While the value of $\Delta\alpha$ can be obtained by RSMs and corresponding L scans, the value of rotation angle ω can be estimated by half-integer X-ray diffraction (HIXRD). For samples with $x = 12$ and 32 u.c., the typical HIXRD results are displayed in Fig. 4(d) and 4(e), where the (1 1/2 3/2) peak corresponds to the in-phase "+" rotation along the a-axis and (1/2 3/2 5/2) to the out-of-phase "–" rotations along the b- and/or c-axis [56,57]. Because the LCMO (CRO) layer has the relatively larger (smaller) lattice constant along the (001) direction, the half-integer peaks of LCMO (CRO) layer are expected to be located on the left (right) side. Take an example with $x = 32$ u.c.; the LCMO rotation angles are fitted by $\omega_a \sim 7.4^\circ$, $\omega_b \sim 8.4^\circ$, and $\omega_c \sim 5.2^\circ$. Compared to $\tan|\Delta\alpha| \sim 0.012$ obtained from the $x = 12$ u.c. sample, the close value of $\sin\omega_b \times \sin\omega_c \sim 0.013$ quantitatively proves the connection between lattice tilting and OOR in perovskite heterostructures with coherent growth (see Supplemental Material Fig. S11 [38]). On the other hand, the $x = 12$ u.c. sample exhibits no observable half-integer peak for LCMO, revealing the simultaneous suppression of lattice tilting ($\Delta\alpha \sim 0.04^\circ$) and OOR ($\omega \sim 0^\circ$). These experimental results and analysis support that the anomalous lattice tilting at the LCMO/CRO interface could be achieved via OOR engineering without breaking the coherent growth. However, the OOR and octahedral deformation (e.g., Jahn–Teller distortion) usually coexist in a strained perovskite oxide layer [58], and possibly further affect lattice tilting.

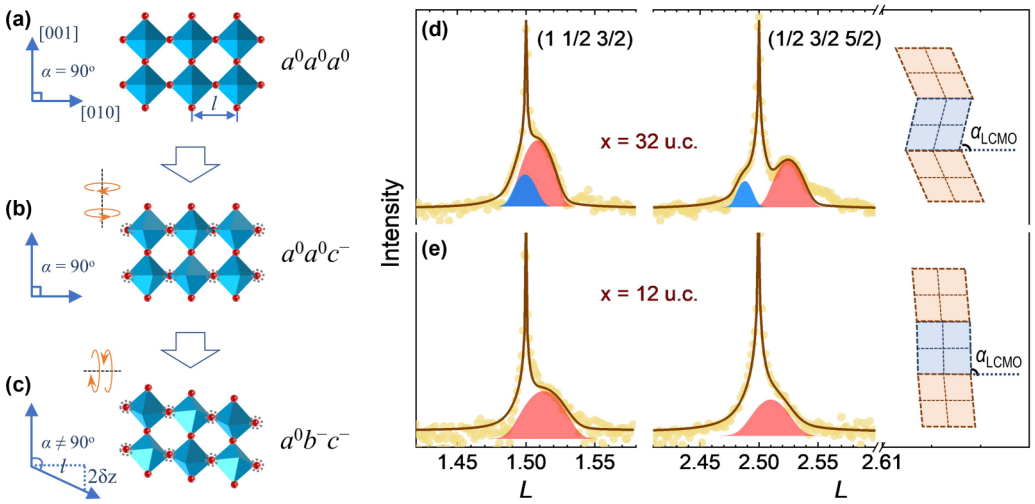

FIG. 4. OOR-related lattice tilting. The monoclinic-like lattice tilting can be induced from a nonrotated oxygen octahedral network in (a) by applying the out-of-phase "–" rotation along the *c*-axis in (b), and then the "–" rotation along the *b*-axis in (c). The HIXRD scans around (1 1/2 3/2) and (1/2 3/2 5/2) are plotted for trilayers with $x = 32$ u.c. in (d) and $x = 12$ u.c. in (e). Insets indicate the corresponding monoclinic-like lattice tilting in the heterostructure.

D. Lattice-Tilting-mediated Magnetic Coercivity

After discussing the possible mechanism for unconventional lattice tilting, we move to the correlation between the magnetic coercivity (H_C) and monoclinic-like lattice tilting (α). By comparing the trilayers with different x in Fig. 3, the reduction on H_C seems to be consistently coupled with the enhancement of monoclinic-like lattice tilting, or the decreasing $\alpha < 90°$. Previous reports have shown that not only the buffer layer thickness x, but also the capping layer thickness y can influence the OOR [59,60]. Thus, the lattice tilting of the CRO/LCMO/CRO trilayers can be also modified by changing y. As sketched in Fig. 5(a), increasing y (i.e., from 6 to 16 u.c.) strengthens the monoclinic-like lattice tilting of LCMO ($\Delta\alpha$ from 0.66° to 0.75°), evidenced by the more asymmetric (0±13) reflections in Supplemental Material Fig. S12 [38]. Therefore, lattice tilting of a sandwiched LCMO can be tuned by changing x and y, providing more samples to examine the relationship between H_C (H_S) and α. If using (x, y) to represent different trilayers for simplicity, Fig. 5(b) and 5(c) displays the reduction on H_C from 86 to 58 Oe (70 to 26 Oe) when increasing y in the samples from (24, 6) to (24, 16) [(32, 6) to (32, 16)]. Moreover, if summarizing all the H_C and α obtained from various interface-engineered LCMO layers, Fig. 5(d) demonstrates that H_C is consistently reduced by the decreasing α with $\alpha \leqslant 90°$. This trend is also maintained for H_S that represents the strength of ferromagnetic coupling.

Based on these experimental data, we discuss the linkage between H_C (H_S) and the monoclinic-like lattice tilting of the ABO_3 lattice. First of all, it is well known that H_C is not only determined by magnetic factors including ferromagnetic coupling strength, magnetic anisotropy, and magnetic domains, but also it is sensitive to nonmagnetic factors such as sample shape and interfacial defects [61–63]. Owing to the same growth conditions, the sample shape and interfacial defect

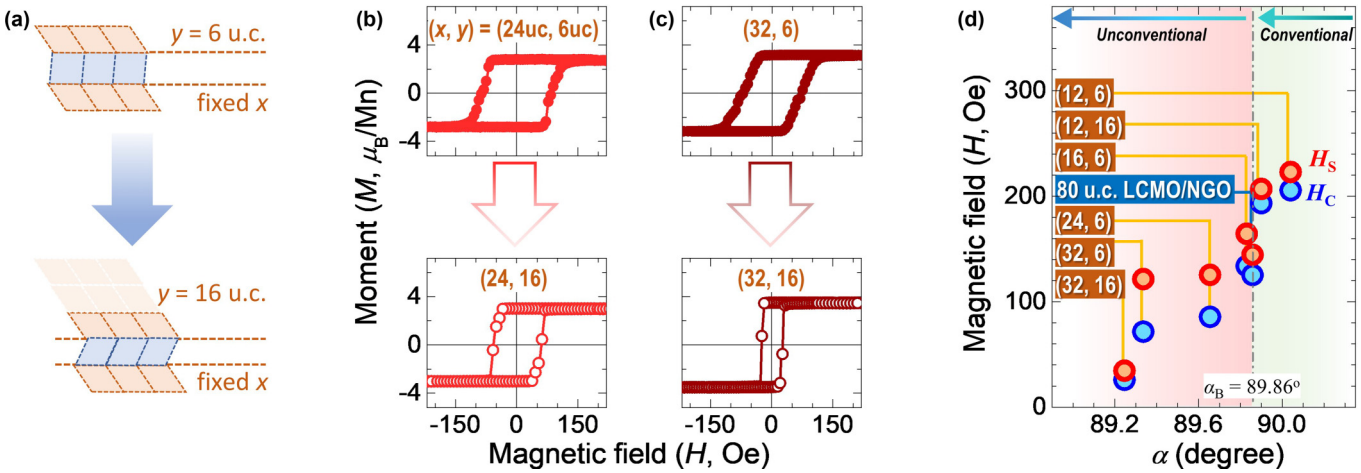

FIG. 5. The monotonic reduction of magnetic coercivity on decreasing α. (a) The sketches for the monoclinic-like lattice tilting in trilayers with different y. (b) M-H loops measured at 150 K for four samples: (24, 6), (24, 16), (32, 6) and (32, 16). (c) H_C and H_S plotted as a function of α obtained from different trilayers. The 80-u.c. LCMO//NGO sample with bulk-like α has been added for reference.

density are expected to be similar in all samples, excluding the nonmagnetic factors in affecting H_C. Second, the magnetic anisotropy energy is found to be similar (only within a 2% to 3% difference; see Supplemental Material Fig. S13 [38]) in samples with the large difference in H_C (increased by $\sim$ 200%, from 70 to 205 Oe), thus leaving the ferromagnetic coupling strength and domains as factors affecting H_C. Third, the ferromagnetism of LCMO/CRO is controlled by the Mn-O-Mn and Mn-O-Ru interactions, where the bond angles of Mn-O-Mn and Mn-O-Ru play an important role [39,64]. In the double-exchange scenario, the magnetic coupling strength is closely related to the bandwidth w, which is proportional to $\cos[(\pi-\varphi)/2]$, with φ being the bond angle [65–67]. Meanwhile, the OOR, which is indexed by the rotation angle ω, can simultaneously induce the monoclinic-like lattice tilting with $\tan|\Delta\alpha| = \tan|90^\circ-\alpha| = \sin\omega_b \times \sin\omega_c$ and reduce φ via $\sin(\varphi/2) \sim \cos^2\omega$ [37,68]. Following this idea, the LCMO layer, which shows more intensive monoclinic-like lattice tilting (with the smaller $\alpha < 90^\circ$), shall exhibit the weaker ferromagnetic coupling, accompanied by the smaller energy barriers between different spin states and thus smaller switching fields. For an ideal square M-H loop, the switching field can be directly viewed as H_C (H_S), while in the nonideal, less-square-shaped M-H loops, H_C and H_S correspond to the mean and maximum value of switching fields, respectively, in a multidomain ferromagnet. Therefore, the relationship between α and H_C (H_S) in Fig. 5(d) can be qualitatively explained in terms of lattice-tilting-mediated ferromagnetic coupling. However, the fact that all our trilayer samples show different H_C but similar T_C, probably due to the similar charge transfer of LCMO/CRO, cannot be fully explained via our model. And the quantitative relationship between α and H_C (H_S) is still lacking because of different sizes of magnetic domains in the strained LCMO layer [6,69]. Future work shall be made both experimentally and theoretically to clarify the entire physics picture beneath these interfacial phenomena.

IV. CONCLUSION

In summary, the evolution of new lattice tilting, which is against the conventional concept of structural evolution in epitaxial layers, is experimentally demonstrated in the CRO-engineered LCMO thin layers. The crystal-twinning model of using the heterointerface like the twinning plane is proposed to explain the formation of the twin-like lattice symmetry across the LCMO/CRO interface. More interestingly, the magnetic interaction of the LCMO layer is closely related to lattice tilting, characterized by the consistently reduced H_C (H_S) on decreasing $\alpha < 90^\circ$. Our work delivers important information for designing novel heterostructures and paves a new path to tunable magnetic interactions in oxide heterostructures without changing the epitaxial strain.

ACKNOWLEDGMENTS

This work was supported by the National Natural Science Foundation of China (Grants No. 12074001, No. 12104002, and No. 12104008) and the Singapore Ministry of Education Academic Research Fund Tier 2 (Project No. MOE2018-T2-1-019). The authors acknowledge the Singapore Synchrotron Light Source (SSLS) for providing the facility necessary for conducting the research.

[1] F. M. Granozio, G. Koster, and G. Rijnders, MRS Bull. **38**, 1017 (2013).
[2] D. Yi, N. P. Lu, X. G. Chen, S. C. Shen, and P. Pu, J. Phys. Condens. Matter **29**, 443004 (2017).
[3] Z. Huang, A. Ariando, X. R. Wang, A. Rusydi, J. S. Chen, H. Yang, and T. Venkatesn, Adv. Mater. **30**, 1802439 (2018).
[4] R. Ramesh and D. G. Schlom, Nat. Rev. Mater. **4**, 257 (2019).
[5] M. Dawber, K. M. Rabe, and J. F. Scott, Rev. Mod. Phys. **77**, 1083 (2005).
[6] Z. Huang, L. F. Wang, P. F. Chen, G. Y. Gao, X. L. Tan, B. W. Zhi, X. F. Xuan, and W. B. Wu, Phys. Rev. B **86**, 014410 (2012).
[7] D. G. Schlom, L. Q. Chen, C. J. Fennie, V. Gopalan, D. A. Muller, X. Q. Pan, R. Ramesh, and R. Uecker, MRS Bull. **39**, 118 (2014).
[8] B. Rivas-Murias, I. Lucas, P. Jiménez-Cavero, C. Magén, L. Morellón, and F. Rivadulla, Nano Lett. **16**, 1736 (2016).
[9] C. Dietl, S. K. Sinha, G. Christiani, Y. Khaydukov, T. Keller, D. Putzky, S. Ibrahimkutty, P. Wochner, G. Logvenov, P. A. Van Aken, B. J. Kim, and B. Keimer, Appl. Phys. Lett. **112**, 031902 (2018).
[10] Y. Yokoyama, Y. Yamasaki, M. Taguchi, Y. Hirata, K. Takubo, J. Miyawaki, Y. Harada, D. Asakura, J. Fujioka, M. Nakamura, H. Daimon, M. Kawasaki, Y. Tokura, and H. Wadati, Phys. Rev. Lett. **120**, 206402 (2018).
[11] J. H. Van Der Merwe, J. Appl. Phys. **34**, 123 (1963).
[12] D. X. Ji, S. H. Cai, T. R Paudel, H. Y. Sun, C. C. Zhang, L. Han, Y. F. Wei, Y. P. Zang, M. Gu, Y. Zhang, W. P. Gao, H. X. Huyan, W. Guo, D. Wu, Z. B. Gu, E. Y. Tsymbal, P. Wang, Y. F. Nie, and X. Q. Pan, Nature **570**, 87 (2019).
[13] G. H. Dong *et al.*, Science **366**, 475 (2019).
[14] D. Pesquera, E. Parsonnet, A. Qualls, R. Xu, A. J. Gubser, J. Kim, Y. Z. Jiang, G. Velarde, Y. L. Huang, H. Y. Hwang, R. Ramesh, and L. W. Martin, Adv. Mater. **32**, 200378 (2020).
[15] S. S. Hong, M. Q. Gu, M. Verma, V. Harbola, B. Y. Wang, D. Lu, A. Vailionis, Y. Hikita, R. Pentcheva, J. M. Rondinelli, and H. Y. Hwang, Science **368**, 71 (2020).
[16] Q. Jin *et al.*, Adv. Mater. **33**, 2005920 (2021).
[17] Q.W. Shi, E. Parsonnet, X. X. Cheng, N. Fedorova, R. C. Peng, A. Fernandez, A. Qualls, X. X. Huang, X. Chang, H. R. Zhang, D. Pesquera, S. Das, D. Nikonov, I. Young, L. Q. Chen, L. W. Martin, Y. L. Huang, J. Íñiguez, and R. Ramesh, Nat. Commun. **13**, 1110 (2022).
[18] X. Deng *et al.*, Matter **4**, 1323 (2021).
[19] R. J. Zeches *et al.*, Science **326**, 977 (2009).
[20] R. Gao, A. C. P. Jain, S. Pandya, Y. Q. Dong, Y. K. Yuan, H. Zhou, L. R. Dedon, V. Thoréton, S. Saremi, R. Xu, A. Luo, T. Chen, V. Gopalan, E. Ertekin, J. Kilner, T. Ishihara, N. H. Perry, D. R. Trinkle, and L. W. Martin, Adv. Mater. **32**, 1905178 (2020).

[21] H. Boschker, J. Kautz, E. P. Houwman, W. Siemons, D. H. A. Blank, M. Huijben, G. Koster, A. Vailionis, and G. Rijnders, Phys. Rev. Lett. **109**, 157207 (2012).

[22] A. Vailionis, W. Siemons, and G. Koster, Appl. Phys. Lett. **93**, 051909 (2008).

[23] G. Y. Gao, Z. Z. Yin, Z. Huang, S. W. Jin, and W. B. Wu, J. Phys. D Appl. Phys. **41**, 152001 (2008).

[24] J. M. Rondinelli and N. A. Spaldin, Adv. Mater. **23**, 3363 (2011).

[25] J. M. Rondinelli, S. J. May, and J. W. Freeland, MRS Bull. **37**, 261 (2012).

[26] H. J. Liu, Y. Q. Dong, D. W. Xu, E. Karapetrova, S. Lee, L. Stan, P. Zapol, H. Zhou, and D. D. Fong, Adv. Mater. **30**, 1804775 (2018).

[27] Y. K. Yuan, Y. F. Lu, G. Stone, K. Wang, C. M. Brooks, D. G. Schlom, S. B. Sinnott, H. Zhou, and V. Gopalan, Nat. Commun. **9**, 5220 (2018).

[28] Y. D. Gu, Y. W. Wei, K. Xu, H. R. Zhang, F. Wang, F. Li, M. S. Saleem, C. Z. Chang, J. R. Sun, C. Song, J. Feng, X. Y. Zhang, W. Liu, Z. D. Zhang, J. Zhu, and F. Pan, J. Phys. D Appl. Phys. **52**, 404001 (2019).

[29] Y. Zhou, S. Kouser, A. Y. Borisevich, S. T. Pantelides, and S. J. May, Adv. Mater. Interfaces **7**, 1901576 (2020).

[30] S. G. Jeong, G. Han, S. Song, T. Min, A. Y. Mohmed, S. Park, J. Lee, H. Y. Jeong, Y. M. Kim, D. Y. Cho, and W. S. Choi, Adv. Sci. **7**, 2001643 (2020).

[31] W. W. Li, B. Zhu, Q. He, A. Y. Borisevich, C. Yun, R. Wu, P. Lu, Z. Qi, Q. Wang, A. Chen, H. Wang, S. A. Cavill, K. H. L. Zhang, and J. L. MacManus-Driscoll, Adv. Sci. **7**, 1901606 (2020).

[32] D. Kan, R. Aso, R. Sato, M. Haruta, H. Kurata, and Y. Shimakawa, Nat. Mater. **15**, 432 (2016).

[33] M. S. Li, Z. Huang, C. Tang, D. Song, T. P. Mishra, A. Ariando, T. Ventakesan, C. J. Li, and S. J. Pennycook, Adv. Funct. Mater. **29**, 1906655 (2019).

[34] P. F. Chen, Z. Huang, M. S. Li, X. J. Yu, X. H. Wu, C. J. Li, N. Bao, S. W. Zeng, P. Yang, L. L. Qu, J. S. Chen, J. Ding, S. J. Pennycook, W. B. Wu, T. V. Venkatesan, A. Ariando, and G. M. Chow, Adv. Funct. Mater. **30**, 1909536 (2020).

[35] Z. Liao, M. Huijben, Z. Zhong, N. Gauquelin, S. Macke, R. J. Green, S. V. Aert, J. Verbeeck, G. V. Tendeloo, K. Held, G. A. Swtzky, G. Koster, and G. Rijnders, Nat. Mater. **15**, 425 (2016).

[36] A. M. Glazer, Acta Cryst. **A31**, 756 (1975).

[37] M. Brahlek, A. K. Choquette, C. R. Smith, R. Engel-Herbert, and S. J. May, J. Appl. Phys. **121**, 045303 (2017).

[38] See Supplemental Material at http://link.aps.org/supplemental/10.1103/PhysRevMaterials.6.094414 for additional information on structural (X-ray diffraction, reflection high-energy electron diffraction) and magnetic (temperature-dependent magnetic moment, field-dependent magnetic moment, magnetic anisotropy energy) properties.

[39] P. F. Chen, B. B. Chen, X. L. Tan, H. R. Xu, X. F. Xuan, Z. Guo, F. Jin, and W. B. Wu, Appl. Phys. Lett. **103**, 262402 (2013).

[40] L. Vesylechko, L. Akselrud, W. Morgenroth, U. Bismayer, A. Matkovskii, and D. Savytskii, J. Alloy. Compd. **297**, 46 (2000).

[41] A. Vailionis, H. Boschker, W. Siemons, E. P. Houwman, D. H. Blank, G. Rijnders, and G. Koster, Phys. Rev. B **83**, 064101 (2011).

[42] Z. Z. Yin, Z. Huang, G. Y. Gao, W. B. Wu, G. Y. Wang, and Y. J. Wang, Phys. D Appl. Phys. **42**, 062004 (2009).

[43] W. L. Lu, P. Yang, W. D. Song, G. M. Chow, and J. S. Chen, Phys. Rev. B **88**, 214115 (2013).

[44] A. J. Ying, C. E. Murray, and I. C. Noyan, J. Appl. Cryst. **42**, 401 (2009).

[45] D. Pesquera, X. Marti, V. Holy, R. Bachelet, G. Herranz, and J. Fontcuberta, Appl. Phys. Lett. **99**, 221901 (2011).

[46] G. Y. Gao, S. W. Jin, and W. B. Wu, Appl. Phys. Lett. **90**, 012509 (2007).

[47] B. B. Chen, P. F. Chen, H. R. Xu, X. L. Tan, F. Jin, Z. Guo, B. W. Zhi, and W. B. Wu, Appl. Phys. Lett. **104**, 242416 (2014).

[48] H. Wang, J. Zhu, X. W. Zhang, Y. X. Tang, and H. S. Luo, Appl. Phys. Lett. **92**, 132906 (2008).

[49] C. Wang, X. Ke, J. Wang, R. Liang, Z. Luo, Y. Tian, D. Yi, Q. Zhang, J. Wang, X. F. Han, G. V. Tendeloo, L. Q. Chen, C. W. Nan, R. Ramesh, and J. Zhang, Nat. Commun. **7**, 10636 (2016).

[50] K. J. Katayama, T. Shimizu, O. Sakata, T. Shiraishi, S. Nakamura, T. Kiguchi, A. Akama, T. J. Konno, H. Uchida, and H. Funkubo, J. Appl. Phys. **119**, 134101 (2016).

[51] J. R. Kim, J. Jang, K. J. Go, S. Y. Park, C. J. Roh, J. Bonini, J. Kim, H. G. Lee, K. M. Rabe, J. S. Lee, S. Y. Choi, T. W. Noh, and D. Lee, Nat. Commun. **11**, 4944 (2016).

[52] E. R. Hoglund, D. L. Bao, A. O'Hara, S. Makarem, Z. T. Piontkowski, J. R. Matson, A. K. Yadav, R. C. Haislmier, R. Engel-Herbert, J. F. Ihlefeld, J. Ravichandran, R. Ramesh, J. D. Caldwell, T. E. Beechem, J. A. Tomko, J. A. Hachtel, S. T. Pantelides, P. E. Hopkins, and J. M. Howe, Nature **601**, 556 (2022).

[53] Y. H. Chu, Q. Zhan, L. W. Martin, M. P. Curz, P. L. Yang, G. W. Pabst, F. Zavaliche, S. Y. Yang, J. X. Zhang, L. Q. Chen, D. G. Schlom, I. N. Lin, T. B. Wu, and R. Ramesh, Adv. Mater. **18**, 2307 (2006).

[54] U. Gebhardt, N. V. Kasper, A. Vigliante, P. Wochner, H. Dosch, F. S. Razavi, and H.- U. Habermeier, Phys. Rev. Lett. **98**, 096101 (2007).

[55] S. W. Jin, G. Y. Gao, Z. Huang, Z. Z. Yin, X. Zhang, and W. B. Wu, Appl. Phys. Lett. **92**, 261901 (2008).

[56] A. M. Glazer, Acta Cryst. **B28**, 3384 (1972).

[57] P. M. Woodward, Acta Cryst. **B53**, 32 (1997).

[58] A. Miniotas, A. Vailionis, E. B. Svedberg, and U. O. Karlsson, J. Appl. Phys. **89**, 2134 (2001).

[59] Z. L. Liao, N. Gauquelin, R. J. Green, S. Macke, J. Gonnissen, S. Thomas, Z. C. Zhong, L. Li, L. Si, S. V. Aert, P. Hansmann, K. Held, J. Xia, J. Verbeeck, G. V. Tendeloo, G. A. Sawatzky, G. Koster, M. Huijben, and G. Rijnders, Adv. Funct. Mater. **27**, 1606717 (2017).

[60] P. F. Chen, Z. Huang, C. J. Li, B. M. Zhang, N. Bao, P. Yang, X. J. Yu, S. W. Zeng, C. H. Tang, X. H. Wu, J. S. Chen, J. Ding, S. J. Pennycook, A. Ariando, T. V. Venkatesan, and G. M. Chow, Adv. Funct. Mater. **28**, 1801766 (2018).

[61] D. Grant, M. Ryan, and A. Biswas, Eur. Phys. J. B **91**, 197 (2018).

[62] J. M. D. Coey, Engineering **6**, 119 (2020).

[63] H. G. Wang, G. Laskin, W. W. He, H. Boschker, M. Yi, J. Mannhart, and P. A. V. Aken, Adv. Funct. Mater. **32**, 2108475 (2022).

[64] B. B. Chen, H. R. Xu, C. Ma, S. Mattauch, D. Lan, F. Jin, Z. Guo, S. Y. Wan, P. F. Chen, G. Y. Guan, F. Chen, Y. X. Su, and W. B. Wu, Science **357**, 191 (2017).

[65] C. Zener, Phys. Rev. **82**, 403 (1951).

[66] A. J. Millis, P. B. Littlewood, and B. I. Shraiman, Phys. Rev. Lett. **74**, 5144 (1995).

[67] M. Medarde, J. Mesot, P. Lacorre, S. Rosenkranz, P. Fischer, and K. Gobrecht, Phys. Rev. B **52**, 9248 (1995).

[68] A. T. Zayak, X. Huang, J. B. Neaton, and K. M. Rabe, Phys. Rev. B **74**, 094104 (2006).

[69] A. S. Mcleod, J. D. Zhang, M. Q. Gu, F. Jin, G. Zhang, K. W. Post, X. G. Zhao, A. J. Mills, W. B. Wu, J. M. Rondinelli, R. D. Averitt, and D. N. Basov, Nat. Mater. **19**, 397 (2020).